Optimal Energy Storage System-Based Virtual Inertia Placement: A Frequency Stability Point of View

Hêmin Golpîra, Azin Atarodi, Shiva Amini, Arturo Roman Messina, *Fellow, IEEE*, Bruno Francois, *Senior Member, IEEE*, and Hassan Bevrani, *Senior Member, IEEE*

***Abstract*—In this paper, the problem of optimal placement of virtual inertia is considered as a techno-economic problem from a frequency stability point of view. First, a data driven-based equivalent model of battery energy storage systems, as seen from the electrical system, is proposed. This experimentally validated model takes advantage of the energy storage system special attributes to contribute to inertial response enhancement, via the virtual inertia concept. Then, a new framework is proposed, which considers the battery storage system features, including annual costs, lifetime and state of charge, into the optimal placement formulation to enhance frequency response with a minimum storage capacity. Two well-known dynamical frequency criteria, the frequency nadir and the rate of change of frequency, are utilized in the optimization formulation to determine minimum energy storage systems. Moreover, a power angle-based stability index is also used to assess the effect of virtual inertia on transient stability. Sensitivity and uncertainty analyses are further conducted to assess the applicability of the method. The efficiency of the proposed framework is demonstrated on a linearized model of a three-area power system as well as two nonlinear systems. Simulation results suggest that the proposed method gives improved results in terms of stability measures and less ESS capacity, when compared with other methods proposed in the literature.**

***Index Terms*—Optimal placement, frequency nadir, virtual inertia, energy storage systems, inertial response, rate of change of frequency, transient stability, uncertainty analysis, sensitivity analysis.**

Nomenclature

δ^s	Mechanical rotor angle (*rad*)
ω^s	Mechanical rotor angular speed (*rad/s*)
ω_0	Rated angular speed (*rad/s*)
$T_m(t)$	Mechanical input torque (*p.u.*)
$T_e(t)$	Electrical output torque (*p.u.*)
H	Inertia constant of the system (*s*)
h_i	Inertia of ESS in area *i* (*s*)
$h'_{i.\ \min}$	Minimum required ESS inertia, in compliance with RoCof, in area *i* (*s*)
$h''_{i.\ \min}$	Minimum required ESS inertia, in compliance with frequency nadir, in area *i* (*s*)
$I(t)$	Impulse response of the system
$P(n)$	Data sequence of interest
P_{in}	Injected power of ESS to the host grid
K	Number of sinusoidal components in noise
L	Length of $P(n)$
a_k	Magnitude
Φ_k	Initial phase angle
ω_k	Harmonic frequency in radius
A_k	Complex magnitude of the *k*th-harmonic
s_i	Eigenvectors associated with the noise subspace
e	Signal eigenvector
e^U	Complex-conjugate transpose of *e*
C_{cap}	Capital costs (*$/kW*)
C_{PCS}	Power conversion system costs (*$/kW*)
C_{stor}	Storage section costs (*$/kWh*)
C_{BOP}	Power balance costs (*$/kW*)
t_{ch}	Charging /discharging time (*h*)
$C_{O\&M}$	Operation and maintenance costs (*$/kW-yr*)
$C_{R,a}$	Annualized replacement costs (*$/kW-yr*)
$C_{cap,a}$	Annualized total capital costs (*$/kW-yr*)
$C_{LCC,a}$	Annualized life cycle costs (*$/kW-yr*)
CRF	Capital recovery factor
C_R	Replacement costs (*$/kWh*)
$C_{FOM,a}$	Fixed operation and maintenance costs (*$/kW-yr*)
$C_{VOM,a}$	Variable operation and maintenance costs (*$/kWh*)
n_{cycle}	Number of discharge cycles per year
ζ_c	Charging efficiency of the battery (%)
ζ_d	Discharging efficiency of the battery (%)
η	Power angle-based stability index

Manuscript received January 7, 2020; revised March 30, 2020 and May 26, 2020; accepted May 30, 2020. Paper no. TPWRS-00030-2020. *(Corresponding author: Hemin Golpîra.)* Q1

Hêmin Golpîra, Azin Atarodi, Shiva Amini, and Hassan Bevrani are with the Department of Electrical and Computer Engineering, University of Kurdistan, Sanandaj 66177-15175, Iran (e-mail: hemin.golpira@uok.ac.ir; a.atarodi@eng.uok.ac.ir; sh.amini@eng.uok.ac.ir; bevrani@uok.ac.ir, golpira@wisc.edu).

Arturo Roman Messina is with the CINVESTAV, Guadalajara 21573, Mexico (e-mail: arturo.roman@cinvestav.mx).

Bruno Francois is with the Arts et Métiers Paris Tech, HEI, EA 2697-L2EP, Laboratory of Electrical Engineering and Power Electronics, University of Lille, Centrale Lille 59800, France (e-mail: bruno.francois@centralelille.fr).

Color versions of one or more of the figures in this article are available online at https://ieeexplore.ieee.org.

Digital Object Identifier 10.1109/TPWRS.2020.3000324

Q2

I. Introduction

INERTIAL response is defined as the power associated with changes in kinetic energy of synchronous generator rotors, in response to frequency changes, which is fed(taken) to(from) the grid [1]. Before reaction of traditional ancillary control loops, this energy, provided by system inertia, is the key factor to limit the power imbalance. System inertia has a major influence on frequency stability and the associated rate of change of frequency (*RoCoF*) and frequency nadir.

Inverter-based renewable sources are increasingly replacing synchronous generators, which in turn decrease overall system inertia. The ever-growing number of frequency incidents, in response to fluctuations of renewable power sources, accompanied with low level inertia feature jeopardize frequency stability [2]–[4]. This motivates the need to develop advanced ancillary energy balancing services to control frequency changes. Paramount among these, is Virtual Inertia emulation which mitigates undesired frequency dynamics. However, not only insufficient level of inertia, but also its heterogeneous distribution together with time-varying inertia profiles may render frequency dynamics faster. These facts, along with the need to economically keep system secure, make optimal placement of virtual inertia a key factor [2]. This paper addresses the problem of optimal placement of virtual inertia in power grids from a fundamentally new perspective.

Effects of energy storage systems (ESSs) on frequency regulation have been studied in recent research works such as [5]–[7]. They deal with balancing of generation and load to maintain a constant system frequency and to keep tie-line power flows at scheduled values. These studies consider long term frequency response as well as steady state metrics, while neglect inertia requirements and primary frequency as the main metrics utilized for system resilience analysis. Some recent studies have investigated the effect of low system inertia on frequency stability [8]–[14]. In parallel with these efforts, recent research works [15]–[21] demonstrate the way on which virtual inertia could be emulated in different ways, including appropriate control of wind turbines and energy storage systems (ESSs). In [22], an optimization framework to deal with various aspects of inertia emulation and control including how inertia emulation impacts system stability, and determining the best places to add virtual inertia is proposed. Some questions about the heterogeneous inertial profiles and how the associated negative impacts are reduced by inertia emulation has been raised in [11]. Poolla et al. [2] and Farmer et al. [19] focus on H_2 performance metric to determine optimal placement of virtual inertia. Determination of the optimum size of battery to provide the primary frequency control is addressed in [23], [24]. In particular, ESSs do not constantly participate in primary regulation, due to life-time concerns. Instead, in practice, the ESSs are controlled in a hierarchical fashion, dispatched by an optimal function to guarantee the State-of-Charge (SOC) and life-time constraints, which is missed in the so far researches. Some research works, such as [25], deal with optimal placement of virtual inertia in power system considering network structure. It employs DC-power flow to tackle network structure into formulation.

A main limitation of these approaches is the reliance on steady state considerations. It is well known, however, that dynamical frequency indices, such as RoCoF and frequency nadir, are important parameters in assessing frequency stability and the activation of protection schemes. This paper re-formulates the virtual inertia placement problem in term of dynamical metrics. Using this approach, the effects of virtual inertia on the frequency indices can be assessed using a dynamic equivalent model obtained by mapping the electromechanical behavior of ESSs onto a second-order synchronous generator (SG) model. The main contributions of this paper can be summarized as follows:

- An attempt is made to systematically represent the ESS dynamical behavior by a second-order SG model that extends previous work by the authors [15] on the emulation of virtual inertia. Within this framework, a new signal processing technique, called MUltiple Signal Classification (MUSIC) algorithm is developed to derive the model.
- As formulating differential equations in the optimization problem is a hard task, a mathematical framework is proposed to represent dynamical metrics by algebraic inequality constraints. In particular, the present paper describes the complex optimization problem of virtual inertia placement by a new simple formulation.
- Since, the ESSs sizing is a difficult problem in practice, and considering the energy capacity, price, life-time and SOC may not be addressed by the proposed synchronous-based model; an attempt is made to tie the virtual inertia to the ESS features.

II. Virtual Inertia Equivalent Model

A. General Concept

The main step towards optimal placement of virtual inertia in a power grid is to analyze its effects on the frequency stability behavior. This could be visualized by appropriate modelling of the virtual inertia. Generally, providing virtual inertia and thereby contributing to the overall equivalent grid inertia could be achieved by using the virtual synchronous generator (VSG) concept. VSG relies on similar power-balance-based synchronization mechanism as SGs to realize such functionality [26], which would be investigated for modeling purpose in this paper.

With synchronous generation being displaced with modern power electronic based generation such a solar and wind generation, the analysis of inertial response of variable resource generation becomes of fundamental importance. Energy storage systems can, in principle, provide most of its stored energy to support frequency in an interconnected power system and hence a set of large battery ESSs could play the same role as SGs in the inertial response horizon. Conceptually, the charging/discharging process of ESS can be interpreted as the initial compensation of a disturbance by the stored kinetic energy of a SG rotating mass. This means that, while the ESSs would be triggered by a command signal, from frequency measurements, for charging/discharging, a SG model could be used to represent the associated dynamics.

The classical model of a SG is a second-order model of the form

$$\left\{ \begin{array}{l} \dot{\delta}^s = \omega^s \ (t) - \omega_0 \\ H\dot{\omega}^s = T_m\left(t\right) - T_e\left(t\right) \end{array} \right\} \tag{1}$$

where δ^s, ω^s, and ω_0 are the mechanical rotor angle, the mechanical rotor angular speed and the initial angular speed, respectively; H, $T_m(t)$ and $T_e(t)$ are the inertia constant, mechanical input torque and electrical output torque, respectively [27].

Taking the slow electromechanical behavior of the battery ESS into account, the associated dynamics could be represented by (1). The problem of interest, however, is to calculate the equivalent inertia constant and mechanical input torque. To deal with this possibility, a data-driven approach in which uncertain behavior of the ESS is inherently considered to provide complementary information for the swing equation model of (1), is proposed.

B. Data Driven-Based Equivalent Model: To introduce the proposed equivalent model, assume that the injected power of the ESS to the host grid is a discrete-time signal *P*(*n*) of length *L*. Let the time-varying signal *P*(*n*) be decomposed into *K* sinusoidal components in noise, as [28], [29]:

$$P\left(n\right) = \sum_{k=1}^{K} a_k \cos\left(n\omega_k + \Phi_k\right) + w\left(n\right) \tag{2}$$

where, a_k, Φ_k, ω_k and *w(n)* are the magnitude and the initial phase angle, harmonic frequency in radius and additive white noise, respectively. In the model, a_k and ω_k are assumed to be deterministic and unknown, and Φ_k is unknown and assumed to be random and uniformly distributed in $[-\pi, \pi]$. Alternatively, the model (2) can be expressed in the form of noisy complex exponentials as [19]

$$P\left(n\right) = \sum_{k=1}^{K} A_k e^{(jn\omega_k)} + w\left(n\right) \tag{3}$$

where $A_k = |A_k| e_k^{j\Phi}$ is the complex magnitude of the *k*th-harmonic(noise) signal component. As the MUSIC algorithm is a noise subspace-based method, it is a good tool to deal with experimental noisy measured signals. Using this framework, the dimensional space is divided into signal and noise components, which is of high importance to accurately calculate *H* and $T_m(t)$ in (1).

The MUSIC method employs a harmonic model and estimates the frequencies and powers of the harmonics in the signal. Application of the MUSIC method to the data sequence, *P*(*n*), gives:

$$P_{MUSIC}\left(e^{j\omega}\right) = \frac{1}{\sum_{i=K+1}^{M} |e^{U} s_i|^2} \tag{4}$$

where the s_i are the eigenvectors associated with the noise subspace that are orthogonal to the signal eigenvector $e = [1\, e^{j\omega}\, ej^{2\omega}\, e^{j(M-1)\omega}]^{\mathrm{T}}$, and e^{U} denotes the complex-conjugate transpose; *M* is the dimension of space spanned by *P*(*n*). It is worth emphasizing that $P_{MUSIC}(e^{j\omega})$ in (4) does not relate to any real power spectrum; rather, the only purpose of this pseudo-spectrum is to generate peaks whose frequencies correspond to those of the dominant frequency components. This feature makes the MUSIC approach interesting to develop equivalent model based on dominant modes.

For a given signal of interest and according to (2)–(4), eigenvalues would be calculated. By knowing the eigenvalues and because the impulse response is the inverse Laplace transform of eigenvalues, one could represent a signal of interest with a pre-defined model of (1). For this purpose, suppose the impulse response of system is *I*(*t*); for the input signal *x*(*t*), i.e. $x(t) = T_m(t)$ in (1), one could write *y*(*t*), i.e. $\dot{\omega}$, as:

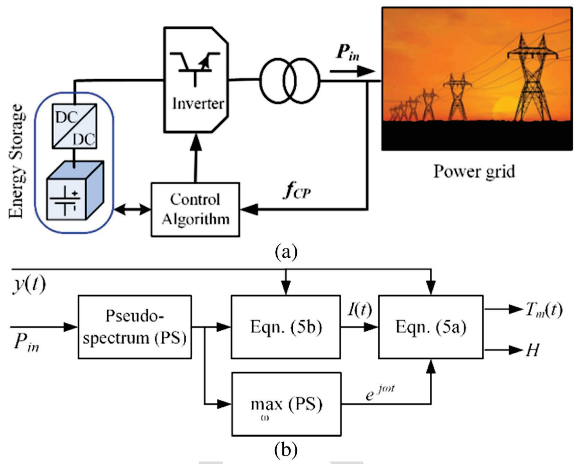

Fig. 1. Block diagram representation of the proposed modeling process: (a) virtual inertia emulation mechanism, and (b) the proposed equivalent model; P_{in}, *y(t) and* f_{cp} represent the grid injected power, the frequency deviation of the ESS, and the frequency at the point of connection of the ESS, respectively.

$$y\left(t\right) = x\left(t\right) \int_{t=0}^{\infty} I\left(t\right) e^{j\omega t} dt \tag{5.a}$$

where,

$$I(t) = y(t) * PS \tag{5.b}$$

and *PS* in (5.b) is the pseudo-spectrum of the signal. Equation, (5.b) reveals that *I*(*t*) results from convolution of *y*(*t*) and PS.

In the modelling procedure and by measuring the output response of the system *y*(*t*) and by knowing *I*(*t*), the problem of interest is to calculate *x*(*t*) in (5). By calculating $T_m(t)$, the ESS could be replaced by the synchronous generator model of (1). Using this approach, *o* in (5.a) is defined as the dominant frequency components of the pseudo-spectrum in (4).

Figure 1 gives a schematic illustration of this model. In this plot, Fig. 1(a) illustrates the process of virtual inertia emulation using the battery ESS, while Fig. 1(b) describes a simplified block diagram representation of the proposed equivalent model. The input to the control algorithm is the frequency at the connection point of the inverter f_{cp}, and P_{in} represents the grid injected power.

C. Model Validation: The efficiency of the proposed method is illustrated using the existing battery ESS in the University of Kurdistan Micro-Grid (UOK-MG). Fig. 2 shows a three-phase diagram representation of the UOK-MG. Details of the physical UOK-MG are given in [30].

Figure 3 shows the battery ESS and the main grid power variation behavior, i.e. P_{in} in Fig. 1, recorded for the UOK-MG. As shown in Fig. 3, Event 1 triggers the charging process of the ESS in response to deviations from the minimum SOC.

The main grid power deviation during the charging process in Fig. 3 is utilized to calculate the Pseudo-spectrum (see Fig. 4) which, in turn, is used to estimate the dominant frequency components in (4).

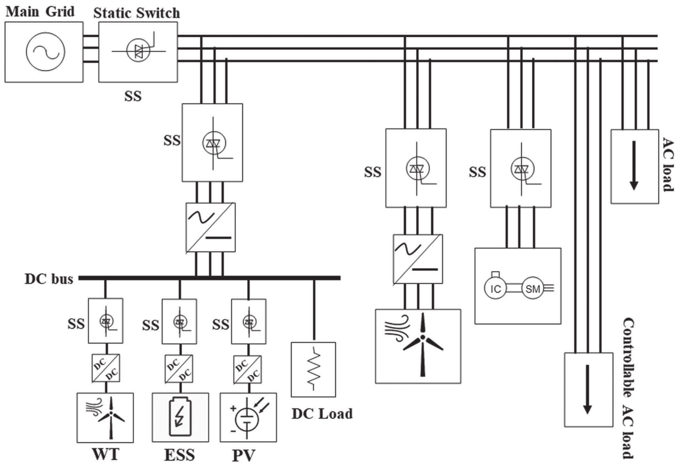

Fig. 2. Three-phase schematic representation of the UOK-MG.

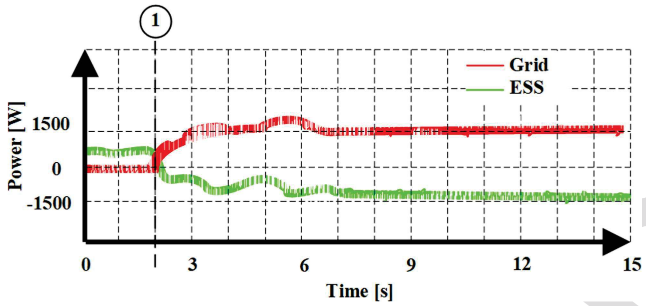

Fig. 3. The ESS and grid experimental dynamic responses.

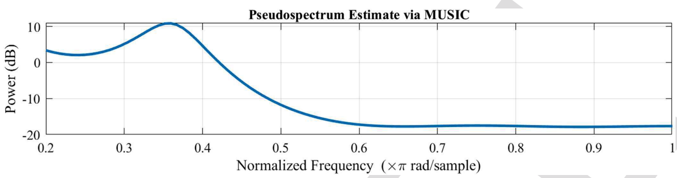

Fig. 4. The Pseudospectrum estimation via MUSIC.

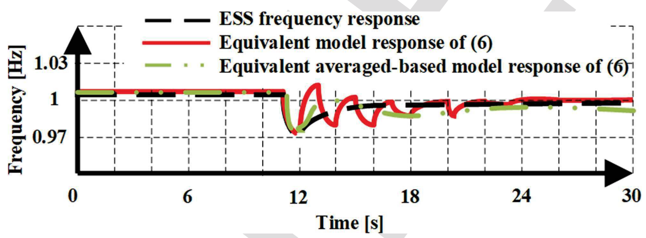

Fig. 5. Comparison of frequency response computed from the experiment and the equivalent frequency response models.

Setting the frequency deviation of the ESS in Fig. 5 as $y(t)$ and the Pseudo-spectrum of Fig. 4 as PS for (5) gives:

$$\left\{ \begin{array}{l} \dot{\delta}^s = \omega^s - \omega_0 \\ 0.53\dot{\omega}^s = \left(1 - e^{-0.38t}\right) C - T_e\left(t\right) \end{array} \right\} \quad (6)$$

where, C is a constant value and would be set to fit the DC term in (4). In interpreting this model, note that constant 0.38 in (6) represents the dominant frequency of the Pseudo-spectrum in Fig. 4 which would be fed to (5) to calculate the 0.53 s inertia constant in (6). Figure 5 demonstrates the effectiveness of the equivalent model (6) to approximate the inertial response behavior of the ESS. To exactly mimic frequency behavior of ESS using (6), the oscillatory behavior of the adopted model would be removed using a 20-samples rolling-averaging window. This approach averages the long-term oscillations, and hence, mitigates the oscillatory behavior beyond the inertial response horizon.

Results in Fig. 5 show that the dynamic behavior of ESS, especially in the inertial response horizon can be approximated by a simple SG model. It should be emphasized that while a conventional SG is slower and less flexible compared to ESS, developed dynamical equivalent model of ESSs in the grid connected mode is not only affected by the fast-inherent features of ESSs but also is significantly influenced by the external zone, i.e. the host grid, features.

III. Optimization Problem

This section formulates the ESS placement as an optimal techno-economic problem.

A. *Costs of Energy Storages and Technologies*

There are two main approaches for assessing the cost of storage technologies: 1) Total Capital Cost (TCC), and 2) Life Cycle Cost (LCC) [31]. For the sake of generality of the method, no specific ESS technologies are considered in this section.

In the TCC approach, all terms associated with the purchase, installation, and delivery of the ESS units, including Power Conversion System (PCS) costs (C_{PCS}), costs of ESS (C_{stor}), and cost of balance of plant (C_{BOP}), are considered as:

$$C_{cap} = C_{PCS} + C_{BOP} + C_{stor} \times t_{ch} \quad (\$/kW) \quad (7)$$

where t_{ch} is the charging /discharging time. The balance of the ESS, known as the BOP, includes site wiring, interconnecting transformers, and other additional ancillary equipment and is measured on a \$/kW basis [32].

However, the LCC is a more common metric to evaluate and compare different ESS technologies. The annualized LCC is formulated according to (8) which considers operation and maintenance costs ($C_{o\&M,a}$), replacement cost ($C_{R,a}$) and annualized TCC.

$$C_{LCC,a} = C_{cap,a} + C_{O\&M,a} + C_{R,a} \quad (\$/kW - yr) \quad (8)$$

in which:

$$CRF = \frac{i(1+i)^T}{(1+i)^T - 1} \quad (9)$$

$$C_{cap,a} = TCC \times CRF \quad (\$/\left(kW - yr\right)) \quad (10)$$

$$C_{O\&M,a} = C_{FOM,a} + C_{VOM,a} \times n_{cycle} \times t_{ch} \quad (\$/kW - yr) \quad (11)$$

$$C_{R,a} = CRF \times \sum_{k=1}^{r} (1+i)^{-kt} \times \left(\frac{C_R \times t_{ch}}{\eta_{sys}}\right) \quad (\$/kW - yr) \quad (12)$$

where *CRF*, *i*, *T*, *r*, *t*, and η_{sys} are the capital recovery factor, interest rate and the life time, the number of substitutions in lifetime, the replacement period and the overall efficiency, respectively; $C_{FOM,a}$ and $C_{VOM,a}$ define the fixed and variable operation and maintenance costs. Subscript "a" stands for "annualized" costs.

B. Formulation of Objective Function and Constraints

Equation (8) specifies the annual cost per kilowatt of the installed ESS in compliance with the lifetime. However, for optimal placement of virtual inertia, it is necessary to rewrite the cost function in (8) according to the amount of virtual inertia.

The synchronous inertia constant (*H*) is defined as the ratio of stored kinetic energy to the rated apparent power of the system, as:

$$H = \frac{0.5 J_{VI}\, \omega^2}{S_{base}} \tag{13}$$

where J_{VI}, ω, and S_{base} are the moment of inertia, angular velocity and rated apparent power, respectively. Since the stored energy in ESSs is usually expressed in volt ampere hour (VAh_{ESS}), it is needed to express the associated value in term of Joule. Considering unity power factor, one could re-write (13) as:

$$KW_{ESS} = KVA_{ESS} = \frac{h_{ESS} S_{base}}{3600\ s} \rightarrow$$
$$h_{ESS} = \frac{3600\ VAsec_{ESS}}{S_{base}} \tag{14.a}$$

This equation gives the average hourly power that can be injected/absorbed to/from the grid by the ESS. To validate such representation, results obtained from (14.a), for frequency response of Fig. 5, are compared with those of well-established methods of calculating inertia. Using the classical swing equation during 500 ms after fault occurrence, one can conventionally calculate inertia constant as [33]:

$$H_{Conv.} = \frac{\Delta P_L}{2 RoCoF_{500ms}} = \frac{\Delta P_L}{2\left(\frac{f(0.5) - f(0)}{0.5}\right)} \tag{14.b}$$

A comparison with the frequency responses of Fig. 5 shows an error of 3.17% which in turn justifies the proposed formulation in (14.a).

By substituting (14.a) into (8), one could write the optimization problem as:

$$\underset{h_i}{\text{minimize}} \quad F(h_i) = \sum_{i=1}^{n_{ESS}} \left(C_{LCC,a\ i} \times \frac{h_i\ S_{base}}{3600\ \text{sec}} \right) \tag{15.a}$$

$$\text{st}: \quad RoCoF_i \leq RoCoF_{\max} \tag{15.b}$$

$$\Delta f_{\text{nadir}\ i} \leq \Delta f_{nadir\ max} \tag{15.c}$$

$$SOC_{\min} \leq SOC_i \leq SOC_{\max} \tag{15.d}$$

where n_{ESS} is the number of ESSs. Moreover, the SOC should remain within an appropriate range which is addressed in (15.d). The SOC can be calculated as follows [34, 35]

$$SOC(\Delta t) = SOC(0) - \frac{\int_0^{\Delta t} \zeta p(t)\, dt}{E_{ESS,rated}} \tag{16.a}$$

where,

$$\zeta = \begin{cases} \zeta_c & P(t) < 0 \\ \frac{1}{\zeta_d} & P(t) > 0 \end{cases} \tag{16.b}$$

and *p*(*t*) is battery power which gets negative values for the charging procedure and positive values for the discharging period; $E_{ESS,rated}$, Δt, ζ_c, and ζ_d are the nominal energy capacity, charge/discharge time, charging and discharging efficiencies of the battery, respectively.

C. Determining the Bounds of Virtual Inertia

Constraints (15.b) and (15.c) explain that the optimization problem (15) enforces the RoCoF and frequency nadir in all areas to be less than standard values. These terms make the optimization problem difficult to deal with as it depends on dynamical indices. Generally, it is common to specify the lower/upper bounds based on different criteria, including capacity of equipment or budget. Therefore, the problem of interest here is to re-write the upper and lower bounds of (15.b) and (15.c) in terms of the emulated inertia, i.e. *h*.

1) Rate of Change of Frequency: The RoCoF is a meaningful criterion to show ability of a system in the face of a sudden power imbalance. Greater RoCoF means that the less time is available for system operator to arrest frequency decline [36]. Time interval of 100 milliseconds to 2 seconds are defined to measure the RoCoF [36], [37]. ENTSO standard [37] explains that RoCoF is allowed to get a value between 0.5 to 1 Hz/sec.

In order to represent dynamical frequency indices based on lower bounds of inequality constraints of (15.b), the RoCoF would be defined based on the classical swing equation of (1) as [30]:

$$2H \frac{d\Delta f(t)}{dt} = \Delta P_m(t) - \Delta P_L(t) - \Delta P_{tie}(t) \tag{17}$$

Where $\Delta P_m(t)$, $\Delta P_L(t)$, and $\Delta P_{tie}(t)$ represent mechanical power, electrical power and tie line power changes, respectively. Considering the definition of RoCoF, one could write:

$$RoCoF = \frac{\Delta P_m(t) - \Delta P_L(t) - \Delta P_{tie}(t)}{2H} \tag{18}$$

The Taylor series expansion of (18) about the independent variables of *H*, ΔP_m, ΔP_L, and ΔP_{tie} gives

$$\begin{aligned}\Delta RoCoF_i &= \frac{\partial RoCoF_i}{\partial \Delta P_{mi}} \Delta\Delta P_{mi} + \frac{\partial RoCoF_i}{\partial \Delta P_{Li}} \Delta\Delta P_{Li} \\ &+ \frac{\partial RoCoF_i}{\partial \Delta P_{tiei}} \Delta\Delta P_{tiei} + \frac{\partial RoCoF_i}{\partial \Delta H_i} \Delta H_i = \frac{1}{2H_i} \Delta\Delta P_{mi} \\ &+ \frac{-1}{2H_i} \Delta\Delta P_{Li} + \frac{-1}{2H_i} \Delta\Delta P_{tiei} \\ &+ \frac{-\left(\Delta P_{mi} - \Delta P_{Li} - \Delta P_{tiei}\right)}{2{H_i}^2} \Delta H_i\end{aligned} \tag{19}$$

Due to the slow inherent of dynamics of interest, except for the last term of (19), other terms could be neglected. Accordingly, and by replacing (18), one could re-write (19) as:

$$RoCoF_i\left(-\frac{\Delta H_i}{H_i}\right) = \Delta RoCoF_i \tag{20}$$

Considering maximum allowable RoCoF, i.e. $RoCoF_{i,\max}$, the minimum inertia which guarantees the RoCoF to be within the permitted range is calculated as:

$$\begin{aligned} h'_{i,\min} &= \Delta H_{i,\min} \\ &= H_i\left(-\frac{\Delta RoCoF_{i,\max}}{RoCoF_i}\right) \xrightarrow{\Delta RoCoF_{i,\max}=RoCoF_{i,\max}-RoCoF_i} \\ h'_{i,\min} &= H_i\left(-\frac{RoCoF_{i,\max}-RoCoF_i}{RoCoF_i}\right) \end{aligned} \tag{21}$$

where, $h'_{i,\min}$ represents the minimum, in compliance with the RoCof, required inertia which should be emulated by the battery ESS in area *i*. It equals to the difference between the desired inertia to enforce system to follow the standards and the present inertia constant, i.e. $\Delta H_{i,\min}$.

2) Frequency Nadir: Frequency nadir mainly depends on the total inertia of the system and the capability of the power resources to provide primary frequency response [38]. According to NERC and the Union for the Coordination of the Transmission of Electricity (UCTE) standards [39, 40], the minimum allowable frequency that a system could instantaneously experience during the operation is 800 mHz.

Taking the time dependency of the governor response into account, one can write the frequency nadir as [15]:

$$\Delta f_{nadir} = \frac{(\Delta P_L + \Delta P_{tie})^2 T_d}{4HR} \tag{22}$$

where *R* is the extra power received through the governor and T_d is the response time of the governor. In deriving (22), it is assumed that the mechanical power through the governor increases as a linear function of time with the steady gradient R/T_d [41, 42]. While, this is a conservative assumption, Great Britain and Ireland practices show that this is the case for the power increment within 5 and 10 seconds (T_d), respectively, following a contingency [43]. Applying Tayloras expansion to (22) gives

$$\begin{aligned} \Delta\Delta f_{nadir,i} &= \frac{\partial \Delta f_{nadir,i}}{\partial \Delta P_{Li}}\Delta\Delta P_{Li} + \frac{\partial \Delta f_{nadir,i}}{\partial \Delta P_{tie,i}}\Delta\Delta P_{tie,i} \\ &+ \frac{\partial \Delta f_{nadir,i}}{\partial \Delta H_i}\Delta H_i = \frac{(\Delta P_{Li} + \Delta P_{tiei})\,T_{di}}{2H_iR_i}\Delta\Delta P_{Li} \\ &+ \frac{(\Delta P_{Li} + \Delta P_{tiei})\,T_{di}}{2H_iR_i}\Delta\Delta P_{tiei} \\ &+ \frac{-(\Delta P_{Li} + \Delta P_{tiei})^2 T_{di}}{4H_i^2R_i}\Delta H_i \end{aligned} \tag{23}$$

Following the same procedure as that in (21), one could re-write (23) in the form

$$\Delta f_{nadir,i}\left(-\frac{\Delta H_i}{H_i}\right) = \Delta\Delta f_{nadir,\,i} = \Delta(f_{nadir,\,i} - f_0) \tag{24}$$

The minimum inertia, i.e. $h''_{i,\min}$, which guarantees frequency nadir to be in the permitted range is calculated by:

$$\begin{aligned} h''_{i,\min} = \Delta H_{i,\min} &= H_i\left(-\frac{\Delta\Delta f_{nadir\ i,\ max}}{\Delta f_{nadir\ i}}\right) \\ &= H_i\left(-\frac{f_{nadir\ \ max} - \Delta f_{nadir\ i}}{\Delta f_{nadir\ i}}\right) \end{aligned} \tag{25}$$

where, $h''_{i,\min}$ represents the minimum, in compliance with frequency nadir, required inertia which should be emulated by the battery ESS in area *i*. In order to simultaneously satisfy both, frequency nadir and RoCoF standards, the lower bound for virtual inertia in the optimization problem and for each area are selected as the maximum value of (21) and (25), namely:

$$h_{i,\min} = max\left\{h'_{i,\min}, h''_{i,\min}\right\} \tag{26}$$

Moreover, the overall system inertia has a direct impact on the frequency indices. This means that some considerations should be made regarding overall system inertia and, consequently, (21) and (25) would be completed by adding a new equality constraint. For this purpose, the frequency of the overall Center of Inertia (COI), which should satisfy strict frequency standards, would be employed to determine the overall amount of inertia in the system, as [5]:

$$H_{COI} = Q = H\frac{\Delta f_{COI}}{f_{COI}}(61.5) \tag{27}$$

where, Δf_{COI}, and f_{COI} represent the frequency deviation and frequency of the system, without ESS, after the fault, respectively. Formally, equation (27) gives the required amount of inertia constant which guarantees acceptable frequency dynamics of the COI. Of note that *Q* would be realized by adding the emulated inertia of ESSs to the conventional SGs inertia. Accordingly, the optimization problem (15) can be re-written as:

$$\underset{h_i}{\text{minimize}} \quad F(h_i) = \sum_{i=1}^{n_{ESS}}\left(C_{LCC,a\ i}\frac{h_i\ S_{base}}{3600\ \text{sec}}\right) \tag{28.a}$$

$$\text{st:} \quad H_{COI} = Q \tag{28.b}$$

$$h_{i,\min} \le h_i \ \le h_{i,\max} \tag{28.c}$$

$$SOC_{\min} \le SOC_i \le SOC_{\max} \tag{28.d}$$

where the dynamic inequality constraints (15.b) and (15.c) are re-formulated as the algebraic inequality constraint (28.c) in terms of the inertia constant. This dramatically increases the simplicity and speed of the calculations.

IV. Solution Algorithm

In this section, a framework that incorporates the model (6) and the objective function (28) to optimally place battery ESS in the system is proposed.

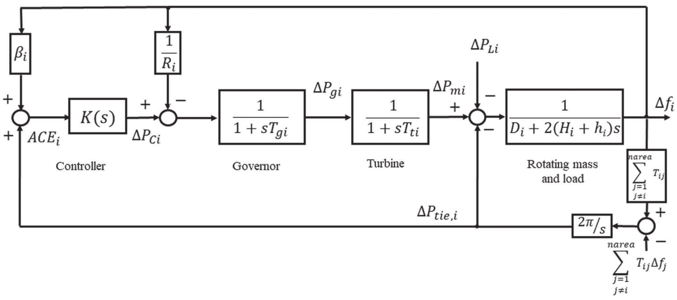

Fig. 6. Block diagram representation of control area i. β_i, R_i, T_{gi}, T_{ti}, and D_i are frequency bias, droop characteristic, governor time constant, turbine time constant, and damping property, respectively.

The algorithm consists of 4 main steps:

Step 1: Define PV buses of the system as candidates for battery ESSs placement;

Step 2: Assume the proposed model (6), with unknown inertia constant, in each PV bus;

Step 3: Define the emulated inertia constant, i.e. h, as a decision variable of the objective function (28). Set C in (6) as the product of the ratio of h to the inertia constant of the installed SG, in the associated bus, and the mechanical power of the SG;

Step 4: Apply a Genetic Algorithm (GA) to solve the minimization problem (28). Indeed, the GA determines the amount of virtual inertia in each PV bus of the system.

V. Simulation and Results

Three test systems have been used for evaluating the proposed formulation in this paper: a) a linearized model of a three-area power system, b) a nonlinear yet simple two-area, four-machine test system, and c) a large scale16-machine, five-area 68-bus test model of the New York/New England system.

A. Linear System

As a first motivating example, a linearized model of a three-area power system is used to assess the efficiency of the proposed formulation. The block diagram of each area is shown in Fig. 6.

Firstly, a 0.2 per unit load disturbance is applied at areas 1 and 3. As a first scenario, the required virtual inertia is calculated only based on (28.b) and arbitrary realized, through the proposed model in (6), in area 1. For simulation purposes, it is assumed that the ESS would be triggered upon occurrence of the fault. Comparison of frequency dynamics for the system with and without virtual inertia reveals that while areas 1 and 2 frequency nadirs improved by means of virtual inertia, area 3 shows an undesired behavior. This in turn numerically justifies the need for optimal inertia placement. Within this framework, (28) may be written as:

$$\underset{h_i}{\text{minimize}} \quad F(h_i) = \sum_{i=1}^{n_{ESS}} \left(C_{LCC,a\,i} \frac{h_i\, S_{base}}{3600 \text{ sec}} \right) \tag{29.a}$$

$$\text{st:} \qquad H_{COI} = 0.053 \tag{29.b}$$

TABLE I
Optimization Results in Three Area System

Method	*h1*	*h2*	*h3*	*F(h$_i$)*
PM*	0.016	0	0.037	2.5916
Ref. [2]	0.023	0.016	0.022	3.0942
Ref. [44]	0.012	0.009	0.038	2.8735

a.PM: Proposed Method

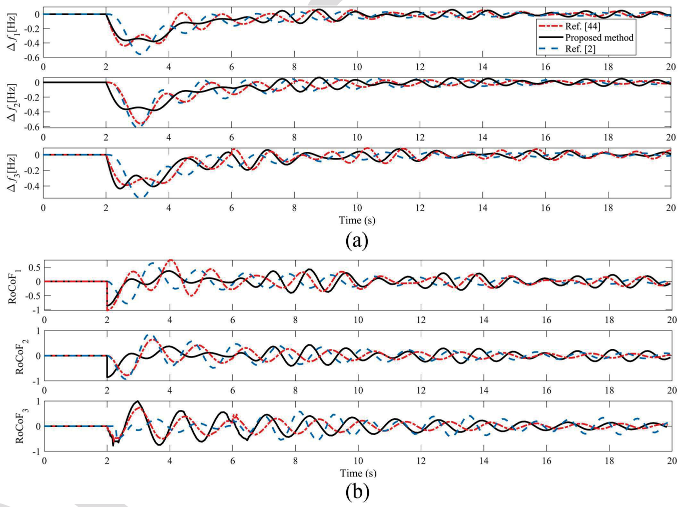

Fig. 7. (a) Frequency behaviors and (b) RoCoF of generators 1, through 3 of three area power system for three cases: proposed formulation, Ref. [44] and Ref. [2].

$$0.0129 \leq h_1 \tag{29.c}$$

$$0 \leq h_2 \tag{29.d}$$

$$0.0225 \leq h_3 \tag{29.e}$$

$$30\% \leq SOC_i \leq 80\% \tag{29.f}$$

where, for instance, the minimum inertia of area 1 in (29.c) is calculated based on (21),(25), and (26) as:

$$h'_{1,\min} = 0.08335 \times \left(-\frac{1 + 1.1870}{-1.1870} \right) = 0.0129$$

$$h''_{1,\min} = 0$$

$$h_{1,\min} = \max\{0, 0.0129\} = 0.0129 \tag{30}$$

Note that some other unspecified parameters of (29) would be set as described in Appendix A. The results obtained, using a simple GA with 0.05 and 0.8 mutation and crossover coefficients, respectively, from optimization of (29) are shown in Table I. In order to further assess efficiency of the proposed formulation, Table I compares the results with those of obtained from [2] and [44]. Comparison results justify the fact that dynamic behavior of ESS could significantly affect optimal placement problem which is missed in previous research.

Figure 7 compares the frequency behavior and RoCoF of generators 1, 2 through 3 for three cases of interest: a) with virtual inertia and according to the proposed formulation, b) with virtual inertia and according to [44], and c) with virtual inertia and according to [2]. It can be seen that while frequency traces

TABLE II
MODAL ANALYSIS OF THE SYSTEMS WITH VI

Method	PM	Ref. [2]	Ref. [44]
Damping	0.2762	0.1265	0.2634

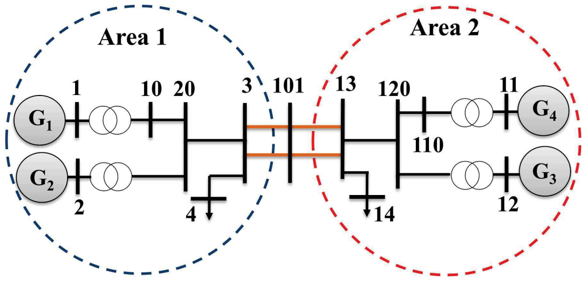

Fig. 8. Single-line diagram of two area system.

TABLE III
OPTIMIZATION RESULTS IN TWO AREA SYSTEM

Method	*h1*	*h2*	*h3*	$F(h_i)$
PM	0.402	0.567	0.004	4.6705
Ref. [2]	0.116	0.332	0.376	6.3104
Ref. [44]	0.212	0.315	0.316	5.7891

TABLE IV
FREQUENCY INDICATORS OF TWO AREA SYSTEM BEFORE AND AFTER APPLICATION OF OPTIMAL INERTIA VALUES

G_i	Without VI		With VI (PM)		With VI [2]		With VI [44]	
	$RoCoF$ (Hz/s)	Δf_{nadir} (Hz)	$RoCoF$ (Hz/s)	Δf_{nadir} (Hz)	$RoCoF$ (Hz/s)	Δf_{nadir} (Hz)	$RoCoF$ (Hz/s)	Δf_{nadir} (Hz)
1	1.187	0.172	0.989	0.143	0.988	0.126	0.973	0.116
2	1.240	0.160	0.989	0.134	0.981	0.112	0.961	0.162
3	0.706	0.267	0.713	0.254	0.730	0.200	0.786	0.198

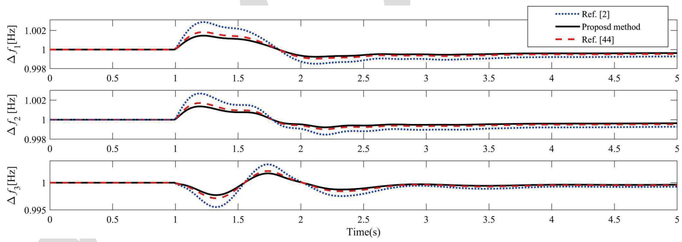

Fig. 9. Frequency response of generators 1, 2 and 3 of the two area power system for three cases: proposed formulation, Ref. [44] and Ref. [2].

of [2], [44] and the proposed method in this paper follow the standards regarding RoCoF and frequency nadir, the proposed formulation results in less ESS capacity.

Also of interest, modal analysis of the results, as explained in Table II, shows the efficiency of the proposed formulation in comparison with that of [2] and [44].

Results show that a lower emulated virtual inertia in the proposed formulation not only decreases the cost function but also causes better performance in terms of enhanced damping.

With virtual inertia, the results from [2] and [44] also seem to perform within the constraints and are almost the same as the results from the proposed method. This could be justified through the fact that set of PV buses for small systems includes a few members to be considered as candidates of ESS installation. Therefore, different algorithms may differ a bit from capacity point of view rather than location which in turn causes negligible difference between the results. To further assess simultaneous effects of virtual inertia on frequency and transient stabilities, two non-linear system are used in what follows.

B. Two-Area Power System

The two-area power system, shown in Fig. 8, is considered to further demonstrate the efficiency of the proposed formulation. Modeling considerations are essentially those described in [45]; all the generating units are modeled with 6$^{\text{th}}$ order synchronous machine models with excitation systems.

The disturbance of interest is the outage of generator G_4, at the first second of simulation. The lower bounds of virtual inertia are calculated according to (29) and (30) as:

$$\underset{h_i}{\text{minimize}} \quad F(h_i) = \sum_{i=1}^{n_{ESS}} \left(C_{LCC,a\,i} \frac{h_i\, S_{base}}{3600 \text{ sec}} \right) \qquad (31.a)$$

$$\text{st}: \quad H_{COI} = 4.973 \qquad (31.b)$$

$$0.3151 \leq h_1$$

$$0.3881 \leq h_2$$

$$0 \leq h_3$$

$$30\% \leq SOC_i \leq 80\% \qquad (31.c)$$

in which, equality constraint of (31.b) reveals:

$$H_{COI} + h_{ESS} = 4.973 \rightarrow h_{ESS} = 4.973 - 4 = 0.973 \qquad (32)$$

Solving (28) leads to the optimum results of Table III. The results also compared with those of optimum virtual inertia of [2] and [44].

Further, Table IV compares frequency stability indices for different approaches. The results demonstrate high efficiency of the proposed method to optimally allocate virtual inertia in the system.

While the frequency nadir of the generators are within the permissible range for the system without virtual inertia, the RoCoFs for the generators 1 and 2 exceed the standard value. Optimal placement of virtual inertia returns generators with undesired frequency dynamics to the normal region. Efficiency of the proposed method is further assessed through time domain simulations of Fig. 9.

Also of interest, effects of virtual inertia on transient stability is assessed using a simple power angle-based stability index η [18]:

$$\eta = \frac{360 - \delta_{\max}}{360 + \delta_{\max}} \qquad (33)$$

where $\delta_{\max}$ is the maximum angle separation between any two generators in the system [46]. Generally stated, the use of simple metrics such as (33) may work for some systems but fail for some others. During severe faults, most ESSs, if remain connected and continue to inject active power which is not the case in many regions, get saturated and cannot follow the frequency properly. Using (33) in this paper relies on a conservative assumption that

TABLE V
TRANSIENTS STABILITY ASSESSMENT

Method	δ_{max}	η
PM	11.02	0.94
Ref. [2]	20.8	0.89
Ref. [44]	16.63	0.91

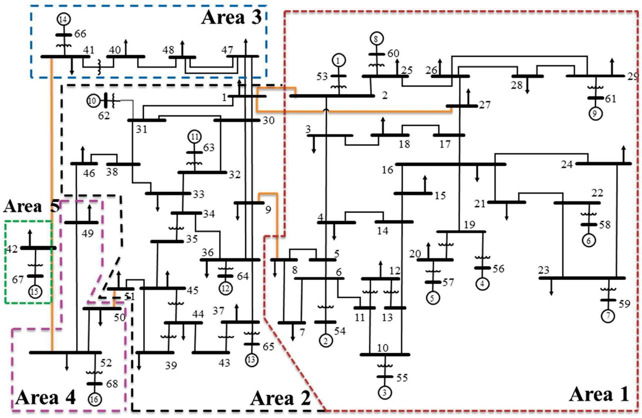

Fig. 10. Single line diagram of the 68-bus system showing coherent areas and their interconnections.

the occurred fault is not a severe one, which causes ESSs to be disconnected from the grid. Moreover, saturation of ESSs in response to sever faults is neglected. Table V demonstrates better performance of the proposed method in comparison with those of [2] and [44].

Note in these results, that a higher value of *** corresponds to a more favorable transient stability condition.

C. New York/New England System

The New England test system is used to further illustrate the efficiency of the proposed algorithm for large scale power systems. A single-line diagram of the system, showing major coherent areas and their interconnections, is shown in Fig. 10.

Five different contingency scenarios, including tripping of major generating units and load shedding, are considered. Results in Table VI compare the proposed algorithm results with those of [2] and [44]. The results show high efficiency of the proposed method to improve frequency dynamics with minimum cost.

Also of interest, Fig. 11 shows the allocation of virtual inertia among the PV buses of the system.

Moreover, Fig. 12 compares the frequency behavior of the system, in response to the outage of generator n1 (scenario 1), for the proposed method, [2] and [44]. It should be noted that while there are negligible deviations between the traces in Fig. 12, significant differences between the cost functions justify the efficiency of the proposed method.

Results show that the optimization problem works better and more effectively for larger areas. This can be understood by noting that set of PV buses for large areas includes many members to be considered as candidates for ESS placement. As a result, there are a lot of possibilities for both the size and location.

TABLE VI
OPTIMIZATION RESULTS IN NEW YORK/NEW ENGLAND SYSTEM

		h_1	h_2	h_3	h_4	h_5	$F(h_i)$
1	PM	0.412	0.432	0.313	0.092	0.111	9.2141
	Ref. [2]	0.506	0.332	0.376	0.201	0.112	12.4031
	Ref. [44]	0.378	0.453	0.306	0.115	0.098	11.0817
2	PM	0.341	0.513	0.209	0.101	0.098	10.8601
	Ref. [2]	0.340	0.712	0.301	0.113	0.160	13.0012
	Ref. [44]	0.300	0.798	0.251	0.098	0.161	12.3140
3	PM	0.474	0.261	0.160	0.261	0.007	9.7516
	Ref. [2]	0.596	0.298	0.267	0.271	0.088	11.2113
	Ref. [44]	0.314	0.351	0.294	0.314	~0	10.0087
4	PM	0.169	0.203	0.617	0.135	0.072	9.8617
	Ref. [2]	0.132	0.512	0.694	0.196	0.209	10.5103
	Ref. [44]	0.100	0.374	0.687	0.096	0.101	10.0102
5	PM	0.613	0.032	0.116	0.076	~0	9.0412
	Ref. [2]	0.743	0.215	0.402	0.031	~0	9.9731
	Ref. [44]	0.412	0.354	0.391	0.116	~0	9.4019

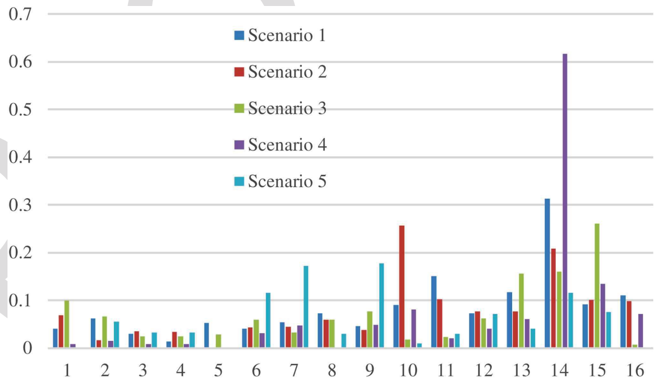

Fig. 11. Virtual inertia allocation for New-England system.

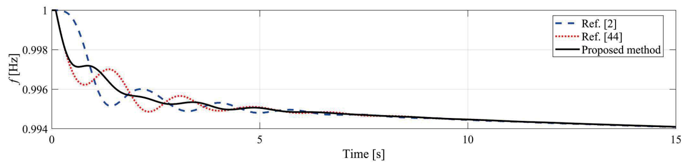

Fig. 12. Frequency responses of New England system for different approaches.

Moreover, the efficiency of the proposed formulation to enhance transient stability is shown in Table VII, using (33).

Table VII shows that appropriate placement of virtual inertia in the system, considering dynamical behavior of ESS, could also improve transient stability. This could be justified through the fact that the so far researches, e.g. [2], rely on quasi-steady state phasors for voltages and currents in transient stability assessment. In other words, they consider constant nominal value of frequency in defining system impedances which is far from realistic for system with penetration of inverter based ESSs. This point is successfully addressed in the proposed formulation by explicitly representing the dynamic behavior of ESSs in the problem formulation.

TABLE VII
OPTIMIZATION RESULTS IN NEW ENGLAND SYSTEM

	Method	η_{12}	η_{13}	η_{14}	η_{15}	η_{25}	η_{35}
1	PM	0.92	0.87	0.91	0.89	0.90	0.89
	Ref. [2]	0.85	0.84	0.91	0.90	0.85	0.87
	Ref. [44]	0.87	0.86	0.91	0.89	0.88	0.88
2	PM	0.98	0.83	0.92	0.93	0.95	0.95
	Ref. [44]	0.94	0.82	0.91	0.90	0.91	0.92
	Ref. [2]	0.91	0.84	0.90	0.88	0.89	0.95
3	PM	0.87	0.90	0.90	0.89	0.92	0.92
	Ref. [44]	0.85	0.88	0.90	0.88	0.88	0.88
	Ref. [2]	0.88	0.85	0.87	0.87	0.87	0.88
4	PM	0.96	0.93	0. 93	0.93	0.93	0.93
	Ref. [44]	0.96	0.90	0.91	0.93	0.92	0.89
	Ref. [2]	0.95	0.94	0.93	0.93	0.91	0.85
5	PM	0.94	0.85	0.92	0.92	0.91	0.96
	Ref. [44]	0.89	0.86	0.90	0.90	0.89	0.94
	Ref. [2]	0.93	0.87	0.87	0.87	0.88	0.91

VI. SENSITIVITY AND UNCERTAINTY ANALYSIS

In this section, sensitivity analyses are conducted to understand the effect of operation conditions, including variations of faults magnitude, operating point, and annualized LCC on the optimization problem. For this purpose, (28.a) is used to calculate sensitivity of the cost function to operation condition, as:

$$F(h_i) + \Delta F(h_i) = \sum_{i=1}^{n_{ESS}} \left(C_{LCC,a\,i} \frac{h_i\, S_{base}}{3600 \text{ sec}} \right) + \frac{\partial F(h_i)}{\partial \Delta P_L} \Delta\Delta P_L + \frac{\partial F(h_i)}{\partial \Delta P_m} \Delta\Delta P_m + \frac{\partial F(h_i)}{\partial C_{LCC,a\,i}} \Delta C_{LCC,a\,i} \tag{34}$$

Then, according to (19) and (23), one could write the sensitivity matrix (26) as:

$$\begin{bmatrix} \partial h'_{i,\min} \\ \partial h''_{i,\min} \end{bmatrix} = \begin{bmatrix} \frac{\partial RoCoF_i}{\partial \Delta P_{Li}} & \frac{\partial RoCoF_i}{\partial \Delta P_{mi}} \\ \frac{\partial \Delta f_{nadir,i}}{\partial \Delta P_{Li}} & 0 \end{bmatrix} \begin{bmatrix} \Delta\Delta P_{Li} \\ \Delta\Delta P_{mi} \end{bmatrix} \tag{35}$$

Considering (35) in (34) gives:

$$\begin{aligned} \Delta F(h_i) &= \frac{\partial F(h_i)}{\partial h_i} \frac{\partial h_i}{\partial \Delta P_L} \Delta\Delta P_L + \frac{\partial F(h_i)}{\partial h_i} \frac{\partial h_i}{\partial \Delta P_m} \Delta\Delta P_m \\ &= \sum_{i=1}^{n_{ESS}} \left(C_{LCC,a\,i} \frac{S_{base}}{3600 \text{ sec}} \right) \times \max \left\{ \frac{\partial RoCoF_i}{\partial \Delta P_{Li}} \Delta\Delta P_L \right. \\ &\quad \left. + \frac{\partial RoCoF_i}{\partial \Delta P_{mi}} \Delta\Delta P_m \,,\, \frac{\partial \Delta F_{nadir,i}}{\partial \Delta P_{Li}} \Delta\Delta P_{Li} \right\} \\ &\quad + \sum_{i=1}^{n_{ESS}} \left(\frac{h_i S_{base}}{3600 \text{ sec}} \right) \Delta C_{LCC,a\,i} \end{aligned} \tag{36}$$

The usefulness of (36) is now assessed for the New-England system. For this purpose, contingency 1, i.e. the outage of generator 1 in area 1, is considered as the base case. Cost function for outage of generator 7 in area 1, i.e. scenario 2, and generator 11 in area 2, i.e. scenario 3, are calculated using (36). Table VIII compares the results which clearly justify effectiveness of the proposed sensitivity analysis.

TABLE VIII
SENSITIVITY ANALYSIS

Scenario	Cost function of (28)	Cost function of (35)
2	9.7516	9.5913
3	9.8617	9.9302

For uncertainty analysis, the equality constraint of (28.b) is represented in the objective function (28.a), as:

$$\begin{aligned} \underset{h_i}{\text{minimize}} \quad F(h_i) = \sum_{i=1}^{n_{ESS}} \left(C_{LCC,a\,i} \frac{h_i\, S_{base}}{3600 \text{ sec}} \right) \\ + \beta(H_{COI} - Q) \end{aligned} \tag{37}$$

where *b* is arbitrary chosen high with the aim of enforcing the results to follow the equality constraint of (28.b). Considering parametric uncertainty for inertia constant i.e. H_{COI}, one could write (37) as:

$$\begin{aligned} \underset{h_i}{\text{minimize}}\, F(h_i) &= \sum_{i=1}^{n_{ESS}} \left(C_{LCC,a\,i} \frac{h_i\, S_{base}}{3600 \text{ sec}} \right) \\ &\quad + \beta(H_{COI} + \gamma - Q) \rightarrow \\ \underset{h_i}{\text{minimize}}\, F(h_i) &= \sum_{i=1}^{n_{ESS}} \left(C_{LCC,a\,i} \frac{h_i\, S_{base}}{3600 \text{ sec}} \right) \\ &\quad + \beta(H_{COI} - Q) + \beta\gamma \end{aligned} \tag{38}$$

where *g* expressed in percentage of H_{COI}. To deal with uncertainty analysis, a simple interval approach is utilized. It assumes that the uncertain parameters take value in a specified interval. It could be reinterpreted as the probabilistic modeling with a uniform probability density function (PDF). In this method, the upper and lower bounds for the uncertain inertia parameter are defined. The aim is to find the lower and upper bounds of objective function [47].

Using the proposed framework, assume that the maximum uncertainty of inertia constant is considered to be 5p. This means that the interval of interest can be defined as:

$$\gamma = [H_{COI} - 0.05(H_{COI}),\ H_{COI} + 0.05(H_{COI})] \tag{39}$$

which in turn causes $F(h_i)$ as:

$$F(h_i) = [3.8298,\ 5.5112] \tag{40}$$

with a uniform PDF.

VII. CONCLUSION

While rotational inertia stabilizes the frequency of power grids against small and large disturbances, it leads for oscillations between generators. This paper provides a framework for optimal placement of virtual inertia in low inertia power systems which in turn improves host grid frequency stability. In this way, the ESSs are used to emulate virtual inertia placement. On the other hand, the proposed method in this paper tackles dynamical behavior of the ESSs into problem formulation and thus causes less, in comparison with the literature, virtual inertia to be implemented in the system. This in turn causes better rotor angle stability features. Of note that the proposed algorithm can be a valuable tool in generation expansion planning of power system and inertia deployment.

A data driven-based approach to represent the ESS dynamics using conventional synchronous generator is proposed. This in turn causes the gathered data, from the field setup, provides complementary information to the conventional based model of synchronous generator. Simulation results validate accuracy and efficiency of the proposed modelling procedure.

Using the proposed strategy in a linear three-area power system and two non-linear systems, the required ESS for each area with the lowest cost and capacity are determined. It was found that the calculated values could well maintain the frequency indices within the permissible range. Also, the results showed that the optimal virtual inertia arrangement could have a positive effect on the transient stability and the amount of power exchange between control areas.

Appendix

TABLE IX
ECONOMICAL PARAMETERS RELATED TO THE OPTIMIZATION PROBLEM [25], [26]

Parameter	Value	Parameter	Value
$i(\%)$	8	$C_{FOM,a}$ ($/kw-yr)	10
C_{PSC} ($/kw)	200	$C_{VOM,a}$ ($/kwh)	5
C_{BOP} ($/kw)	50	R	2
C_{stor} ($/kw)	300	$t(yr)$	6
C_R ($/kw)	300	$\eta_{sys}(\%)$	75

TABLE X
TECHNICAL PARAMETERS RELATED TO THE OPTIMIZATION PROBLEM [22], [24].

Parameter	Value	Parameter	Value
S_{base} (MVA)	1000	P_{ESS} (MW)	1
$RoCoF_{max}$ (Hz/s)	1	$E_{ESS,\ rated}$ $(MVAh)$	0.25
$\Delta f_{nadir,max}$ (Hz)	0.8	$\eta_d = \eta_c(\%)$	75
$SOC(0)$	0.5	$t(yr)$	15
SOC_{min}	0.3	$t_{ch}(hrs)$	0.25
SOC_{max}	0.8	n_{cycle}	1000

References

[1] A. Mullane and M. O'Malley, "The inertial response of induction-machine-based wind turbines," *IEEE Trans. Power Syst.*, vol. 20, no. 3, pp. 1496–1503, Aug. 2005.
[2] B. K. Poolla, S. Bolognani, and F. Dörfler, "Optimal placement of virtual inertia in power grids," *IEEE Trans. Autom. Control*, vol. 62, no. 12, pp. 6209–6220, 2017.
[3] H. Bevrani, B. François, and T. Ise, *Microgrid dynamics and control*. Hoboken, NJ, USA: John Wiley & Sons, 2017.
[4] H. Golpîra and A. R. Messina, "A center-of-gravity-based approach to estimate slow power and frequency variations," *IEEE Trans. Power Syst.*, vol. 33, no. 1, pp. 1026–1035, Jan. 2018.
[5] B. Lian, A. Sims, D. Yu, C. Wang, and R. W. Dunn, "Optimizing LiFePO4 battery energy storage systems for frequency response in the UK system," *IEEE Trans. Sustain. Energy*, vol. 8, no. 1, pp. 385–394, Jan. 2017.
[6] Z. Wu, D. W. Gao, H. Zhang, S. Yan, and X. Wang, "Coordinated control strategy of battery energy storage system and PMSG-WTG to enhance system frequency regulation capability," *IEEE Trans. Sustain. Energy*, vol. 8, no. 3, pp. 1330–1343, Jul. 2017.
[7] F. Zhang, Z. Hu, X. Xie, J. Zhang, and Y. Song, "Assessment of the effectiveness of energy storage resources in the frequency regulation of a single-area power system," *IEEE Trans. Power Syst.*, vol. 32, no. 5, pp. 3373–3380, Sep. 2017.
[8] A. S. Ahmadyar, S. Riaz, G. Verbič, A. Chapman, and D. J. Hill, "A framework for assessing renewable integration limits with respect to frequency performance," *IEEE Trans. Power Syst.*, vol. 33, no. 4, pp. 4444–4453, Jul. 2018.
[9] H. Golpîra, H. Seifi, A. R. Messina, and M.-R. Haghifam, "Maximum penetration level of micro-grids in large-scale power systems: Frequency stability viewpoint," *IEEE Trans. Power Syst.*, vol. 31, no. 6, pp. 5163–5171, Nov. 2016.
[10] E. Spahic, D. Varma, G. Beck, G. Kuhn, and V. Hild, "Impact of reduced system inertia on stable power system operation and an overview of possible solutions," in *Proc. IEEE Power Energy Soc. Gen. Meet.*, 2016, pp. 1–5.
[11] A. Ulbig, T. S. Borsche, and G. Andersson, "Impact of low rotational inertia on power system stability and operation," *Int. Federation Accountants Proc. Vol.*, vol. 47, no. 3, pp. 7290–7297, 2014.
[12] Y. Wang, H. Bayem, M. Giralt-Devant, V. Silva, X. Guillaud, and B. Francois, "Methods for assessing available wind primary power reserve," *IEEE Trans. Sustain. Energy* vol. 6, no. 1, pp. 272–280, Jan. 2015.
[13] Y. Wang, G. Delille, H. Bayem, X. Guillaud, and B. Francois, "High wind power penetration in isolated power systems—Assessment of wind inertial and primary frequency responses," *IEEE Trans. Power Syst.*, vol. 28, no. 3, pp. 2412–2420, Aug. 2013.
[14] Z. Chu, U. Markovic, G. Hug, and F. Teng, "Towards optimal system scheduling with synthetic inertia provision from wind turbines," *IEEE Trans. Power Syst.* to be published, 2020. Q4
[15] H. Golpîra, A. R. Messina, and H. Bevrani, "Emulation of virtual inertia to accommodate higher penetration levels of distributed generation in power grids," *IEEE Trans. Power Syst.*, vol. 34, no. 5, pp. 3384–3394, Sep. 2019.
[16] S. D'Arco and J. A. Suul, "Equivalence of virtual synchronous machines and frequency-droops for converter-based microgrids," *IEEE Trans. Smart Grid*, vol. 5, no. 1, pp. 394–395, Jan. 2014.
[17] E. Rakhshani, D. Remon, A. M. Cantarellas, and P. Rodriguez, "Analysis of derivative control based virtual inertia in multi-area high-voltage direct current interconnected power systems," *IET Gener. Transmiss. Distribution*, vol. 10, no. 6, pp. 1458–1469, 2016.
[18] E. Hammad, A. Farraj, and D. Kundur, "On effective virtual inertia of storage-based distributed control for transient stability," *IEEE Trans. Smart Grid*, vol. 10, no. 1, pp. 327–336, Jan. 2019.
[19] W. J. Farmer and A. Rix, "Optimising power system frequency stability using virtual inertia from inverter-based renewable energy generation," in *Proc. Int. Conf. Clean Electr. Power*, 2019, pp. 394–404.
[20] A. Attya, O. Anaya-Lara, and W. Leithead, "Novel concept of renewables association with synchronous generation for enhancing the provision of ancillary services," *Appl. Energy*, vol. 229, pp. 1035–1047, 2018.
[21] B. K. Poolla, D. Groß, and F. Dörfler, "Placement and implementation of grid-forming and grid-following virtual inertia and fast frequency response," *IEEE Trans. Power Syst.*, vol. 34, no. 4, pp. 3035–3046, Jul. 2019.
[22] T. S. Borsche, T. Liu, and D. J. Hill, "Effects of rotational inertia on power system damping and frequency transients," in *54th IEEE Conf. Decis. Control*, 2015, IEEE, pp. 5940–5946.
[23] M. H. Fini and M. E. H. Golshan, "Determining optimal virtual inertia and frequency control parameters to preserve the frequency stability in islanded microgrids with high penetration of renewables," *Electr. Power Syst. Res.*, vol. 154, pp. 13–22, 2018.
[24] A. Oudalov, D. Chartouni, and C. Ohler, "Optimizing a battery energy storage system for primary frequency control," *IEEE Trans. Power Syst.*, vol. 22, no. 3, pp. 1259–1266, Aug. 2007.
[25] S. Wogrin and D. F. Gayme, "Optimizing storage siting, sizing, and technology portfolios in transmission-constrained networks," *IEEE Trans. Power Syst.*, vol. 30, no. 6, pp. 3304–3313, Nov. 2015.
[26] O. Mo, S. D'Arco, and J. A. Suul, "Evaluation of virtual synchronous machines with dynamic or quasi-stationary machine models," *IEEE Trans. Ind. Electron.*, vol. 64, no. 7, pp. 5952–5962, Jul. 2017.
[27] O. Ajala, A. Dominguez-garcia, P. Sauer, and D. Liberzon, "A library of second-order models for synchronous machines," 2018, *arXiv:1803.09707*. Q5
[28] M. H. Bollen and I. Y. Gu, *Signal Processing of Power Quality Disturbances*. Hoboken, NJ, USA: John Wiley a Sons, 2006.
[29] D. G. Manolakis, V. K. Ingle, and S. M. Kogon, *Statistical and Adaptive Signal Processing: Spectral Estimation, Signal Modeling, Adaptive Filtering, and Array Processing*. New York, NY, USA: McGraw-Hill, 2000.

[30] H. Golpîra, "Bulk power system frequency stability assessment in presence of microgrids," *Electric Power Syst. Res.*, vol. 174, 2019, Art. no. 105863.

[31] B. Zakeri and S. Syri, "Electrical energy storage systems: A comparative life cycle cost analysis," *Renewable Sustain. Energy Rev.*, vol. 42, pp. 569–596, 2015.

[32] K. Mongird *et al.*, "Energy storage technology and cost characterization report," *Pacific Northwest National Lab.(PNNL)*. Richland, WA (United Q6 States), 2019.

Q7 [33] *Fast Freq. Response Concepts Bulk Power Syst. Rel. Needs*, NERC, 2020.

[34] I. Teruo, "State of charge calculation device and state of charge calculation method," ed: US Patents, US6845332B2, 2005.

[35] Z. X. Tang and Y. S. Lim, "Frequency regulation mechanism of energy storage system for the power grid," in *Proc. 4th IET Clean Energy Technol.* Q8 *Conf.*, 2016.

[36] J. H. Eto, "Use of frequency response metrics to assess the planning and operating requirements for reliable integration of variable renewable generation," *Ernest Orlando Lawrence Berkeley National Laboratory*. Berkeley, CA: Tech. Rep, LBNL-4142E, 2011.

[37] *Frequency Stability Evaluation Criteria for the Synchronous Zone of Continental Europe –Requirements and impacting factors*. Brussels, Belgium: European Network of Transmission System Operators for Electricity (entsoe), 2016.

[38] Y. Wen, W. Li, G. Huang, and X. Liu, "Frequency dynamics constrained unit commitment with battery energy storage," *IEEE Trans. Power Syst.*, vol. 31, no. 6, pp. 5115–5125, Nov. 2016.

[39] A. Ekwue and B. Cory, "Transmission system expansion planning by interactive methods," *IEEE Trans. Power App. Syst.*, no. 7, pp. 1583–1591, Jul. 1984.

[40] C. E. O. H. ENTSO-E, "P1-Policy 1: Load-frequency control and performance," ed: Tech. Rep. 2000-130-003, May 2000.

[41] H. Chavez, R. Baldick, and S. Sharma, "Governor rate-constrained OPF for primary frequency control adequacy," *IEEE Trans. Power Syst.*, vol. 29, no. 3, pp. 1473–1480, May 2014.

[42] F. Teng, V. Trovato, and G. Strbac, "Stochastic scheduling with inertia-dependent fast frequency response requirements," *IEEE Trans. Power Syst.*, vol. 31, no. 2, pp. 1557–1566, Mar. 2016.

[43] N. Grid. "Security and quality of supply standards," [Online] Available: http://www2.nationalgrid.com/UK/Industry-information/Electricity-codes/System-Security-and-Quality-of-Supply-Standards/ Q9

[44] T. Borsche and F. Dörfler, "On placement of synthetic inertia with explicit time-domain constraints," 2017, *arXiv:1705.03244*.

[45] G. Rogers, *Power System Oscillations*. Berlin, Germany: Springer Science a Business Media, 2012.

[46] P. L. Inc and TSAT, "Transient security assessment tool user manual," Powertech Labs Inc.

[47] M. Aien, A. Hajebrahimi, and M. Fotuhi-Firuzabad, "A comprehensive review on uncertainty modeling techniques in power system studies," *Renewable Sustain. Energy Rev.*, vol. 57, pp. 1077–1089, 2016.